https://doi.org/10.5194/egusphere-2024-3181
Preprint. Discussion started: 3 January 2025

Volcanic emission estimates from the inversion of ACTRIS lidar observations and their use for quantitative dispersion modelling

Anna Kampouri[1,2], Vassilis Amiridis[1], Thanasis Georgiou[1,3], Stavros Solomos[4], Anna Gialitaki[1,5], Maria Tsichla[1,6], Michael Rennie[7], Simona Scollo[8], and Prodromos Zanis[2]

[1]Institute for Astronomy, Astrophysics, Space Applications and Remote Sensing, (IAASARS) National Observatory of Athens, 10560 Athens, Greece.
[2]Department of Meteorology and Climatology, School of Geology, Aristotle University of Thessaloniki, 54124 Thessaloniki, Greece.
[3]Laboratory of Atmospheric Physics, Aristotle University of Thessaloniki, 54124 Thessaloniki, Greece.
[4]Research Centre for Atmospheric Physics and Climatology, Academy of Athens, 10680 Athens, Greece.
[5]Department of Physics and Astronomy, Earth Observation Science Group, University of Leicester, Leicester, UK
[6]Environmental Chemical Processes Laboratory, Department of Chemistry, University of Crete, Greece.
[7]European Centre for Medium-Range Weather Forecasts, Reading RG2 9AX, UK.
[8]Istituto Nazionale di Geofisica e Vulcanologia, Osservatorio Etneo, 95125 Catania, Italy.

Correspondence to: Anna Kampouri (akampouri@noa.gr)

Abstract. Modeling the dispersion of volcanic particles following explosive eruptions is critical for aviation safety. To constrain the dispersion of volcanic plumes and assess hazards, calculations rely on accurate characterization of the eruptions source term e.g., variation of emission rate and column height with time and the prevailing wind fields. This study introduces an inverse modeling framework that integrates a Lagrangian dispersion model with lidar observations to estimate emission rates of volcanic particles released during an Etna eruption. The methodology consists of using the FLEXPART model to generate source-receptor relationships between the volcano and a lidar system that observed the ensuing volcanic plume, which then are used to derive the emission rates using the observational data. We leverage data from the ACTRIS Polly^{XT} lidar that operates at the PANhellenic GEophysical observatory of Antikythera. The inversion algorithm utilizes lidar observations and an empirical a-priori emission profile to estimate the volcanic particle source strength, accounting for altitude and time evolution of the plume. Additionally, to study the impact wind fields have on volcanic ash forecasting, the experiment is repeated using fields that assimilate Aeolus wind lidar data. Our approach applied to the 12 March 2021 Etna eruption, accurately captures a dense aerosol layer between 8 and 12.5 km. Results show a minimal difference of the order of 2 % between the observed and the simulated ash concentrations. The presented inversion algorithm coupled with Aeolus data, optimizes both the vertical emission distribution and Etna emission rates, advancing our understanding and preparedness for volcanic events.

https://doi.org/10.5194/egusphere-2024-3181
Preprint. Discussion started: 3 January 2025

1 Introduction

Volcanic ash constitutes a significant hazard to aviation when it is emitted at aircraft cruising altitudes (9 - 11 km), with potential consequences including aircraft engine failure (Guffanti et al., 2005), inaccurate readings of critical navigational instruments, and reduced visibility due to external aircraft corrosion (Clarkson and Simpson, 2017; ICAO, 2016).

In the case of a volcanic eruption, urgent decisions are necessary to determine safe flight routes and ensure that airborne aircraft land safely. While safety remains the top priority, the grounding and rerouting of flights leads to large financial losses e.g. the 2010 eruption of Eyjafjallajökull in Iceland reportedly cost the airline industry over 1 billion USD (Mazzocchi et al., 2010; Oxford Economics, 2012).

Information on volcanic ash dispersion after an eruption is provided to operators by specialized early warning systems (EWSs) operated by the Volcanic Ash Advisory Centres (VAACs) (Fearnley et al., 2018). These systems are typically relied on deterministic volcanic ash transport and dispersion models (VATDM), to offer short-term forecasts of the volcanic ash cloud. Although VAACs specify the expected location of the ash cloud, they do not provide quantitative information about ash concentration. In the spotlight of the expected rise in the number of flights over volcanically active regions in the near future (as indicated by EUROCONTROL, 2022), the probability of encountering volcanic ash at aircraft cruising altitudes will proportionally increase. Consequently, the challenge is to minimize uncertainties in short-term forecasts of volcanic ash dispersion.

The primary sources of uncertainties in deterministic transport models originate from the eruption source parameters, the various model parameterizations (such as wet deposition), and the driving meteorological conditions (Dacre et al., 2011; Prata and Lynch, 2019; Stohl et al., 2011). Typically, VATDMs require specification of parameters about the volcanic events, including a vertical profile of ash emission rates, particle size distribution, and the ash density (Harvey et al., 2020).

The eruption start time can be estimated through satellite observations or by local Volcano Observatories. Various remote sensing techniques exist to estimate the height of the ash plume (Petersen et al., 2011). Though it should be mentioned, that information that rely on observations from passive sensors practically have limited sensitivity to the ash layer height. Mass eruption rates are typically evaluated using empirical relationships based on observed plume heights (Mastin et al., 2009). However, these empirical relationships often fail to consider secondary factors influencing plume height, such as meteorological conditions. The long-range transport of volcanic particles is influenced by tropospheric and/or stratospheric winds, and particularly the vertical wind shear, which is frequently inaccurately represented in numerous Numerical Weather Prediction (NWP) models (Harvey et al., 2020; Houchi et al., 2010; Stoffelen et al., 2020). The absence of representation of significant physical processes and dependence on empirical relations and data from previous eruptions may result in substantial uncertainties in estimates of the erupted mass.

In Amiridis et al., (2023), it is demonstrated that volcanic ash early warning systems can be significantly enhanced from the assimilation of Aeolus wind fields. Notably, these improvements are most pronounced over under-sampled geographical regions, such as the Mediterranean Sea, as volcanoes are often situated in remote areas lacking surface-based observation

https://doi.org/10.5194/egusphere-2024-3181
Preprint. Discussion started: 3 January 2025

networks. Moreover, the study indicates that the positive effect of Aeolus wind data assimilation is more pronounced in the middle and upper troposphere (mostly between 7 and 15 km), compared to the lower troposphere. This may highlight under-sampling issues, since the in situ observations (like radiosondes) traditionally used for data assimilation, exhibit lower vertical resolution in the upper troposphere (Rennie et al., 2021). Considering that volcanic ash plumes are typically injected in upper-tropospheric and lower-stratospheric heights, their transport is largely influenced by upper tropospheric winds hence accuracy in dispersion modelling is advanced from high accuracy wind fields assimilation.

We specifically focus on the Etna eruption that occurred on 12th of March, 2021, coinciding with the investigations provided by (Amiridis et al., 2023; Kampouri et al., 2023). During this event, Aeolus had a close overpass to Etna, providing valuable observations around the volcano. Additionally, the transported volcanic plume was captured in the region of in the Eastern Mediterranean by the ground-based Polly^{XT} lidar system of the PANhellenic GEophysical observatory of Antikythera (PANGEA-NOA) island, in Greece downwind of Etna volcano. This allows for direct comparisons of observations against forecasts, with and without assimilation of Aeolus data, denoted as “w” and “w/o” Aeolus, respectively (as indicated in the studies by Amiridis et al., 2023; Kampouri et al., 2023).

2 The Case of 12 March–14 March 2021 Etna Volcanic Eruption

2.1 Volcanic Activity

Mt. Etna in Italy, recognized as one of the most active volcanoes on Earth, has undergone significant volcanic activity, particularly since February 2021. During this period, the stratovolcano experienced numerous paroxysmal episodes, leading to frequent tephra and sulfate emissions. A notable event occurred on the 12th of March 2021, marking one of the most powerful lava fountain episodes observed at the South East Crater since 2020 (Calvari et al., 2021). The volcanic activity started with Strombolian-type eruptions around 02:35 UTC, escalating in both frequency and intensity until 07:35 UTC, when surveillance cameras from the Istituto Nazionale di Geofisica e Vulcanologia, Osservatorio Etneo (INGV-OE) (Corradini et al., 2018; Scollo et al., 2019), captured the formation of a sustained lava fountain.

Throughout the paroxysmal phase, the eruptive column gradually reached a height up to 9 km a.s.l. (Figure 1). The variation in the eruption column was detected by the visual surveillance camera at the CUAD in Catania (ECV) calibrated by the INGV-OE (Figure 1). The volcanic plume drifted eastwards under the influence of prevailing westerly winds dominant in the eastern Mediterranean region at the time. According to the Volcano Observatory Notice for Aviation (VONA) messages, the INGV-EO observatory (INGV-EO; Corradini et al., 2018; Scollo et al., 2019) issued a RED warning alert, from 06:18 to 08:44 UTC, on the 12th of March 2021, when the strongest ash emission was observed, while an ORANGE alert was issued at 12:30 UTC when the lava fountain ceased, and the volcanic ash plume was dispersed in the atmosphere (Calvari et al., 2021). Additionally, the eruptive activity resulted in abundant tephra fallout, covering several towns on the east flank of the volcano crater, and a lava flow field expanding on the east and north-east flank. In this study, the cloud heights reported by VONA are used as a-priori information to initialize the volcanic ash dispersion simulations, conducted with the FLEXPART (flexible particle

https://doi.org/10.5194/egusphere-2024-3181
Preprint. Discussion started: 3 January 2025

dispersion) Lagrangian model (Brioude et al., 2013; Pisso et al., 2019; Stohl et al., 2005). The FLEXPART ash transport model is driven by wind fields simulated by the WRF regional meteorological model (version 4) (Skamarock et al., 2019), which, in turn, derives initial and boundary conditions from the ECMWF-Integrate Forecast System (IFS) (ECMWF, 2021) global model (for additional information see Sect. 3.3).

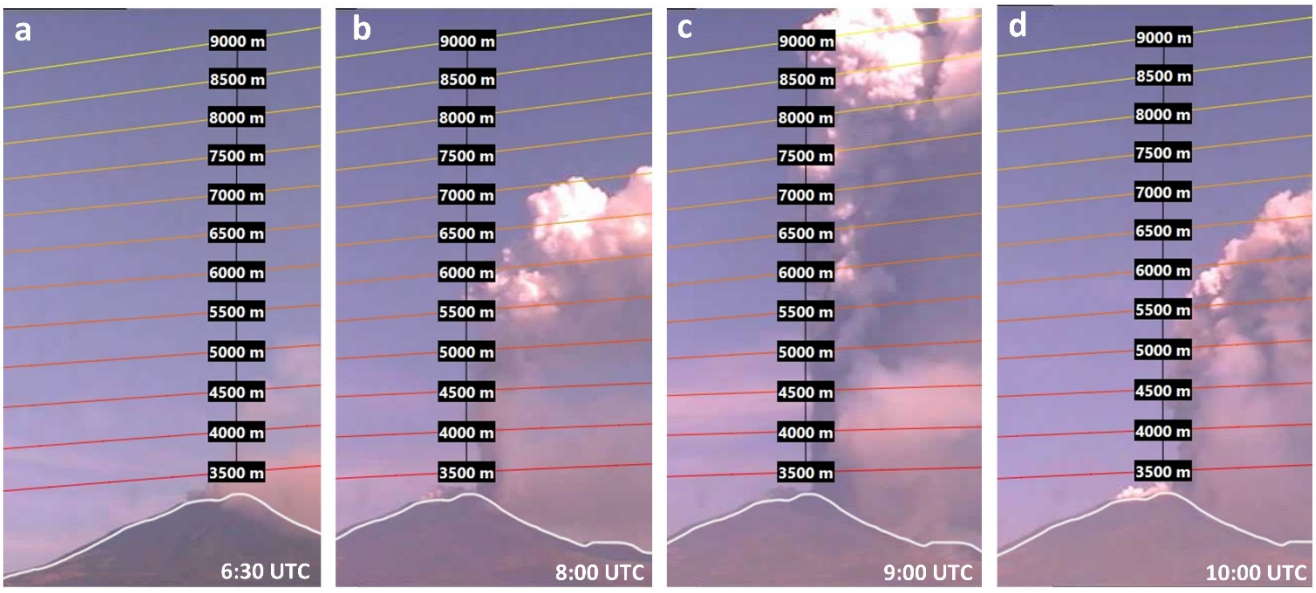

Figure 1: Etna activity on the 12th of March 2021 as seen from INGV-OE. Ash plume images from ECV calibrated camera monitored the explosive volcanic activity between 5 and up to 9 km a.s.l. a) weak ash plume at 06:30, with an upper part aligning more vertically; b) strong vertical plume at 08:00, shifted eastward; c) strong ash plume at 09:00, with a lower and more diluted cloud caused by the lava flow expanding eastward and d) decrease of the explosive activity after 10:00 UTC (figures are taken from Simona Scollo).

3 Methods and Data

The inverse method employed in this study to estimate volcanic ash emissions integrates a-priori information on ash emissions, ground-based lidar observations, and simulations with a dispersion model, resulting in improved ash emission estimates. In this section, we describe the datasets and methods employed in the inverse modeling process.

3.1 PANGEA-NOA ground-based data (Lidar-Polly^{XT})

The PANGEA-NOA observatory established its first operations in June 2018 in the remote island of Antikythera, Greece. The atmospheric circulation pattern at PANGEA-NOA location favours the transport of air masses carrying an abundance of different aerosol types such as windblown Sahara dust, Etna volcanic aerosols, smoke from wildfires and anthropogenic pollution from major megacities. Hence, this coastal site constitutes an ideal place to study natural aerosols under the prevailing background conditions of the Eastern Mediterranean.

https://doi.org/10.5194/egusphere-2024-3181
Preprint. Discussion started: 3 January 2025

Currently, a lidar system the type of Polly^{XT} (Baars et al., 2017; Engelmann et al., 2016) and a sun/sky-photometer of CIMEL Electronique (Giles et al., 2019; Goloub et al., 2007) operate continuously at PANGEA-NOA to provide profiles and columnar aerosol properties with high accuracy and resolution.

Polly^{XT} is a multi-wavelength, Raman, polarization lidar with 24/7 remote operation capability. The system operates in 355, 532 and 1064 nm and is equipped with 12 detectors to measure light elastically and in-elastically (at 387, 407 and 607 nm) backscattered from atmospheric constituents. Polarization capability also enables the detection and vertical separation of non-spherical (e.g., volcanic ash, dust) from spherical aerosols (e.g., smoke, pollution, marine particles).

The CIMEL sun/sky-photometer measures direct solar and sky radiance at several wavelengths (340, 380, 440, 500, 675, 870, 1020 and 1640 nm), to derive column integrated aerosol optical and microphysical properties (Dubovik et al., 2006).

Observations from both sensors are of strong interest for Pan-European ang global networks such as the Aerosol, Clouds and Trace Gases Research Infrastructure (ACTRIS-RI), the European Aerosol Research Lidar Network (EARLINET) and the global AErosol RObotic NETwork (AERONET: https://aeronet.gsfc.nasa.gov/); in all of which measurements taken at PANGEA-NOA are submitted on a regular basis.

3.1.1 Ash mass calculation using remote sensing data

Volcanic ash mass estimates were derived from a combination of Polly^{XT} lidar measurements and sun-photometer observations. First, the lidar measurements were averaged over the 3-hour period when the volcanic layer was observed above Antikythera, and the standardized EARLINET algorithm Single Calculus Chain (SCC) (D'Amico et al., 2015), was used to derive the particle backscatter coefficient (β_p) and particle linear depolarization ratio (δ_p) profiles.

These profiles were then used to disentangle the contribution of large, non-spherical ash particles to the observed volcanic plume and then calculate the ash mass concentration with the "POlarization-LIdar PHOtometer Networking" (POLIPHON) method (Ansmann et al., 2012; Mamouri and Ansmann, 2017), tailored for Etna ash as described in Kampouri et al. (2020). More specifically, the following equation was used:

$$m_a = \rho_a * c_{v,a}(\lambda) * \beta_{p,a}(h,\lambda) * S_{p,a}(h,\lambda), \quad (1)$$

where m is the mass concentration, a indicates an aerosol type, ρ represents the particle mass density, λ is the wavelength, $c_v(\lambda)$ is the so-called volume to extinction conversion factor, derived from sun-photometer measurements and $S_p(\lambda, h)$ is the ratio of the particle extinction to particle backscatter coefficient (lidar ratio).

As m_a calculation is sensitive to the aerosol type, under simultaneous presence of multiple aerosol components in the atmospheric column, a decomposition of the total particle backscatter coefficient $\beta_{p,}$ is needed prior to the mass concentration calculation. In POLIPHON, this decomposition is supported for up to two aerosol types, one exhibiting large particle depolarization ratio values (usually dust or volcanic ash) and one that does not (marine, continental or tropospheric smoke and their mixtures). To separate the contribution of the depolarizing ($\beta_{p.d}(h,\lambda)$) and the non-depolarizing ($\beta_{p.nd}(h,\lambda)$) aerosol component to the total particle backscatter coefficient, we apply the following equations:

https://doi.org/10.5194/egusphere-2024-3181
Preprint. Discussion started: 3 January 2025

$$\beta_{p,d}(h,\lambda) = \beta_p(h,\lambda)\frac{\left(\delta_p(h,\lambda) - \delta_{p,nd}(h,\lambda)\right)\left(1+\delta_{p,d}(h,\lambda)\right)}{\left(\delta_{p,d}(h,\lambda) - \delta_{p,nd}(h,\lambda)\right)\left(1+\delta_p(h,\lambda)\right)}, \quad (2)$$

$$\beta_{p,nd}(h,\lambda) = \beta_p(h,\lambda) - \beta_{p,d}(h,\lambda), \quad (3)$$

Polly^{XT} lidar signals are sensitive to aerosol particles in the radius range from about 50 nm to a few micrometers (Weitkamp, 2005). For FLEXPART, the size range considered for volcanic ash particles is between 5 and 21 μm in diameter, and thus within the range that is detectable from Polly^{XT}. Uncertainties in the ash mass concentration calculation using the POLIPHON method, rise from the input parameters errors that propagate into Eq. (1) and are expected to be in the order of ~40 % (Ansmann et al., 2011). The technique has been validated against synergistic retrievals that combine multi-wavelength lidar and sun/sky-radiometer observations (sensitive up to 15 μm in particle radius (Lopatin et al., 2013, 2021) for dust and volcanic ash particles and has been found to perform well (Konsta et al., 2021; Wagner et al., 2013).

In Table 1, we summarize the values and uncertainties of parameters used as input for the above.

Table 1: Parameters used for lidar profiles decomposition and mass concentration calculation.

	ρ_α [μm cm^{-3}]	$c_{v,\alpha,532nm}$	$\delta_{p,\alpha,532nm}(h)$	$S_{p,\alpha,532nm}(h)$[sr]
Ash particles	2.6 ± 0.6	0.6 ± 0.1	0.36 ± 0.02	50 ± 10
Sulfates	1.5 ± 0.3	0.18 ± 0.04	0.05 ± 0.01	60 ± 20

3.2 Aeolus high spectral resolution lidar (HSRL) data

Aeolus, the European Space Agency's (ESA) wind mission, carried the world's first high spectral resolution Doppler wind lidar (HSRL) placed in space (Stoffelen et al., 2006; Straume-Lindner et al., 2021). Launched in August 2018, Aeolus's aim was to retrieve horizontal wind profiles in the troposphere and lower stratosphere. The mission's primary objective was to showcase this innovative technology in space to enhance weather forecasts and to advance our understanding of atmospheric dynamics, particularly in the tropics. Additionally, Aeolus aimed to contribute valuable insights into the intricate interactions between the atmospheric constituents, water cycles, and the broader climate system (Rennie et al., 2021; Straume-Lindner et al., 2021). Aeolus wind data demonstrated notable quality and coverage, leading to substantial enhancements in NWP forecasts, particularly within the tropics and Southern Hemisphere. The improvement in wind forecasts ranges from 0.5 % to 2 %, maintaining a significant impact even into the medium range. The most substantial impact was observed at approximately 100 hPa in the tropics, particularly over the east Pacific Ocean. This is attributed, in part, to the tropics having a relatively limited coverage of high-quality radiosonde wind profiles. Additionally, the wind field in the tropics is less constrained by temperature information from other satellites (Rennie et al., 2021). Furthermore, Aeolus had the capability to retrieve aerosol and cloud profiles, offering valuable data for assimilation or evaluation in volcanic ash dispersion modeling. It is essential to

https://doi.org/10.5194/egusphere-2024-3181
Preprint. Discussion started: 3 January 2025

note, however, that these retrievals face limitations due to the absence of a dedicated lidar channel for detecting cross-polarized light (with respect to the emitted radiation) returns. This absence is particularly crucial for capturing the backscattered light from non-spherical particles like volcanic ash. Consequently, caution is advised when utilizing Aeolus observations in such cases. Despite this limitation, the Aeolus mission had demonstrated its efficacy in enhancing wind forecasts, particularly over under-sampled regions, such as the tropics (Rennie et al., 2021). Similarly, Aeolus can be used over under-sampled remote areas with active volcanoes, contributing to improved simulations of volcanic ash dispersion following eruptions.

3.3 FLEXPART-WRF model setup

To perform meteorological simulations over the study region of the Eastern Mediterranean the Advanced Research WRF model version 4 (Skamarock et al., 2019) is used. The spatial resolution of the model is 12 × 12 km for a total of 351 × 252 grid points, and 31 vertical levels (up to 50 hPa). The simulation period starts on the 12th of March 2021, at 00:00 UTC (six hours earlier than the FLEXPART runs, to accommodate for the model's spin-up) and ends on the 14th of March 2021, at 18:00 UTC, with hourly outputs. Table 2 summarizes the Physics Parameterizations (PP) schemes for the WRF-ARW simulations.

In the context of this study, two versions (ECMWF, 2021) of the initial and boundary condition fields from the IFS were utilized. These fields, provided at a spatial resolution of 0.125° × 0.125°, with 137 vertical model levels, serve as inputs for the WRF-ARW regional model. One version incorporates assimilated Aeolus Rayleigh-clear and Mie cloudy horizontal line-of-sight (HLOS) L2B wind profiles (referred to as the "w" Aeolus experiment), while the other version is without Aeolus data (referred to as the "w/o" Aeolus experiment). The initial conditions without Aeolus assimilation adhere to the model setup utilized in the Observing System Experiments (OSEs) conducted by (Stoffelen et al., 2006).

The WRF-ARW runs rely on initial and boundary conditions generated from ECMWF-IFS, with boundary conditions being updated at 6-hour intervals. Sea Surface Temperature (SST) analysis data, obtained from the Copernicus Marine Environment Monitoring Service (CMEMS) at a spatial resolution of 1/12°, supplement these simulations. The WRF-ARW model configuration utilized in this study is consistent with that employed in the study of Amiridis et al. (2023).

The volcanic ash plume transport simulations were done with the Lagrangian particle dispersion model FLEXPART (Brioude et al., 2013; Pisso et al., 2019; Stohl et al., 2005) in a forward mode. These simulations rely on hourly meteorological fields from the WRF-ARW model, initiated with IFS datasets. The use of 1-hourly WRF meteorological fields at a 12 × 12 km spatial resolution allow for a more detailed representation of the volcanic plume dispersion. The initial simulations, in which we used an a-priori emission profile for the eruption emissions taken from VONA alerts (from now on referred to as 'a-priori volcanic ash plume transport'), were initiated at the reported start time of the eruption 07:00 UTC on 12th of March 2021 and were completed at 00:00 UTC on 14 March 2021 with a total of 100,000 particles released in each forecast. The model layers were divided into 18 layers with a vertical resolution 1km, in the range extending from 1 to 18 km above ground level (a.g.l.) We estimate the a-priori mass eruption rate (MER) for ash particles following (Degruyter and Bonadonna, 2012; Mastin et al., 2009; Scollo et al., 2019), by inverting the observed plume height using the 1-D plume model of (Degruyter and Bonadonna,

https://doi.org/10.5194/egusphere-2024-3181
Preprint. Discussion started: 3 January 2025

2012). The initial injection height in the model is set to the altitude of the Etna summit craters (3.3 km a.s.l) up to 9 km a.s.l., based on the VONA reports (Corradini et al., 2018; Scollo et al., 2019) and field observations. Also, the gravitational particle settling (Näslund and Thaning, 1991) was determined assuming spherical particles with a density of 2450 kg/m^3. The size distribution of volcanic ash particles was described using four size bins (3, 5, 9, and 21 μm in diameter), as these cover the size distribution relevant for long-range transport (≤ 25 μm diameter) (Beckett et al., 2022; Dacre et al., 2011; Durant et al., 2010).

To derive the source–receptor relationships (SRR), the FLEXPART-WRF model was used once again in a forward mode (see Appendix A, Figure A 1), considering the same four ash size bins as those used in the a-priori volcanic ash plume transport. The SRR model data, which represent all potential dispersion scenarios of the ash plume, are compared with the lidar retrievals at PANGEA-NOA. For each grid point in the considered domain, FLEXPART ash column loadings released from one particular emission time and height are matched with the corresponding time and grid point of the lidar ash mass retrieval.

FLEXPART-SRR were driven by the same hourly meteorological fields from the WRF-ARW model, utilizing both control and assimilated datasets (ECMWF, 2021) to quantitatively evaluate the impact of data assimilation. Subsequently, these SRRs were used to initialize the inversion algorithm, constrained with the Polly^{XT} ground-based lidar measurements of volcanic particles.

It was assumed that the ash emissions occurred between the ground and 16 km a.g.l. over the Etna volcano. The total height range was discretized into 79 layers, each one being 200 m thick. For each layer, 150,000 unit mass particle traces were uniformly released along a vertical line source every two hours (from 04:00 to 06:00 UTC until 12:00 to 14:00 UTC). Additionally, the model layers were divided into 74; 70 layers between 200 m and 14 km, with a vertical resolution of 200 m, 3 layers between 14 and 16 km a.g.l., (per 1 km) and another layer from 22 to 50 km a.g.l. These model-derived column values represent source-receptor relationships, since they were obtained with a unit mass as source. The actual mass released at each level is determined through the inversion. Following the inversion, a single longer 'posteriori' simulation over the period 12 to 14 March 2021 was made releasing 200,000 particles according to the estimated emission profile. The output from this simulation was produced at the same vertical and horizontal resolution as the a-priori FLEXPART simulation.

Table 2: Configuration of the PP schemes for the WRF-ARW simulations.

PP	Schemes	References
Microphysics (MP)	Thompson	(Thompson et al., 2008)
Surface Layer (SFL)	Monin-Obukhov (Janjic Eta)	(Janjic, 2002)
Planetary Boundary layer (PBL)	Mellor-Yamada-Janjic (MYJ)	(Janjic, 2003)
Cumulus Parameterization (CUM)	Tiedtke	(Zhang et al., 2011)
Longwave & Shortwave Radiation (RAD)	Rapid Radiative Transfer Model (RRTMG)	(Iacono, M.J. et al., 2008)
Land Surface (LSM)	NOAH	(Chen, F. and Dudhia, J., 2001)

https://doi.org/10.5194/egusphere-2024-3181
Preprint. Discussion started: 3 January 2025

3.4 Inversion algorithm

The inversion method employed here for ash source estimations is based on a cost function minimization approach. Similar work has been done by (Eckhardt et al., 2008; Kristiansen et al., 2010; Stohl et al., 2011). In these studies, an inversion algorithm was developed to calculate the vertical distribution of sulphur dioxide and ash emission rates for instantaneous volcanic eruptions. Satellite retrievals, typically of ash column loading, have been combined, in those analyses, with VATDM simulations using inversion techniques to provide time-evolving estimates of these significant quantities.

In satellite retrieval techniques, numerous advantages exist where estimates of ash cloud top height and ash column loading are typically available (Francis et al., 2012; Pavolonis et al., 2013). Additionally, mass eruption rates (MER) can be estimated through empirical relationships under specific assumptions, which are especially useful when satellite images are unavailable or limited, such as during the early stages of an eruption (Pouget et al., 2013; Prata et al., 2022). However, direct retrievals of the vertical distribution within the eruption column are not feasible.

The present study brings together: i) the inverse modeling by initiating the inversion simulations with mass concentrations derived from ground-based lidar observations near the source, combined with the source-receptor relationships calculated from the FLEXPART-WRF model, and ii) the use of Aeolus meteorological wind fields (ECMWF, 2021) that are utilized the FLEXPART-WRF model (for more details see Sect. 3.3). The overarching goal is to optimize both the vertical emission distribution, and the ash emission rates near the source, following the volcanic eruption. From the inversion scheme a total ash emission profile of the eruption is obtained, which can be utilized to generate robust ash forecasts constrained by lidar observations.

We perform the inversion using a Bayesian approach to provide the best estimate of the emissions profile for fine ash that can undergo long-range dispersion. We follow the general concept of source-receptor relationships (Seibert and Frank, 2004), where the relations between each measurement and a potential source of the emission is calculated (here using FLEXPART-WRF) and stored as the source-receptor matrix (SRM) for each vertical level and for four ash size bins (as described in Sect. 3.3). The n=79 unknowns (source elements) are put into a state vector x, while the m observed values are put into a vector y_o, where the subscript 'o' stands for the Polly^{XT} lidar observations. Then, the state vector can be calculated from the inversion of a forward model M that connects y_o and x as follows:

$$y_o = M(x) + e_y, \tag{4}$$

implying a linear relationship in which y_o is a vector of spatiotemporal lidar measurements, M is the $m \times n$ SRM calculated by FLEXPART-WRF, describing the sensitivity of each observation to a unit release rate, e_y represents lidar measurement errors and x is the ash emission vector to be estimated. $M(x)$ is equivalent to running a VATDM with x as the input release profile. Since M is calculated using such a model, it inherits the biases that are inevitable in VATDMs. As a result, it may diverge from the true dispersion and may not necessarily align with the observations on the left-hand side of Eq. (4), even if is

https://doi.org/10.5194/egusphere-2024-3181
Preprint. Discussion started: 3 January 2025

the true release profile (Fang et al., 2022). Given that the problem is underdetermined, the solution of the linear inverse problem in Eq. (4) is not straightforward and further assumptions are needed.

The most common are assumptions imposed on the unknown emission vector x such as non-negativity of its elements, smoothness of the emission (Fang et al., 2022) or measurement/emission sparsity (Li et al., 2018), e.g., the assumption that the emission element remains zero unless other evidence is present in measured and modeled data. Under these assumptions, the problem in Eq. (4) can be solved by minimizing the distance between the left and the right sides of the equation. To enhance the stability of the inversion outcome, a-priori emissions are also used, representing our best estimate of x before the observations are made. (are further described in Sect. 3.4.1). Including an explicit a-priori source vector x^a, we can express the equation as follows:

$$M(x - x^a) \approx y_o - Mx^a, \tag{5}$$

and as an abbreviation

$$M\tilde{x} \approx \tilde{y}. \tag{6}$$

The inversion scheme presented here is done by minimizing a cost function C, which comprises the following system of equations:

$$C_1 = y_o - M^T x, \tag{7}$$

$$C_2 = x - x^a, \tag{8}$$

$$C_3 = \epsilon D x, \tag{9}$$

C_1 quantifies the difference between the modeled data and the observations, C_2 the deviation from the a-priori estimations, and C_3 imposes a smoothness regularization term.

The cost function C first calculates the misfit C_1 between the profiles at the receptor points, as observed by the lidar (y_o) and the data as modelled by FLEXPART ($M^T x$).

The second term C_2 Eq. (8) accounts for the difference, between the a-posteriori estimates of the emission rates x and the a-priori estimates x^a (for details on the calculation of the a-priori vector see Sect. 3.4.1). To enforce smoothness in the vertical profile of emissions, a regularization parameter is introduced C_3, derived from a discrete second-order difference operator D Eq. (9). D represents a tridiagonal matrix where the main diagonal elements are equal to −2 and elements of the diagonals above and below equal to 1 (discrete representation of the second derivative), and ϵ is a regularisation parameter that determines the weight of this smoothness constraint relative to the other two terms.

https://doi.org/10.5194/egusphere-2024-3181
Preprint. Discussion started: 3 January 2025

The final mass emission rates are obtained by minimizing the total cost function C using a standard optimization routine with the a-priori emission rates as the initial guess. This approach ensures that the calculated ash emission rates are consistent with both the observed data and the a-priori emissions estimates, while also favoring a smooth vertical distribution of emissions.

3.4.1 A-priori source emissions x^a

To constrain the variability of the retrieved parameters and enhance the stability of the inversion outcome, a-priori emissions are also used inversion scheme. We determine the a-priori mass eruption rate (MER) for ash particles following the approach outlined by (Scollo et al., 2019) by inverting the observed plume heights using the 1-D plume model Degruyter and Bonadonna, (2012) as described in Sect. (3.3). Additionally, the London VAAC employs the same empirical relationship between observed plume heights and eruptive mass as proposed by Mastin et al., (2009), assuming a uniform vertical ash distribution.

The column heights of the ash plume from 12th of March 2021 were obtained from the ECV calibrated camera operated by the INGV-OE (Calvari et al., 2021; Corradini et al., 2018; Scollo et al., 2019) during the period from 6:30 to 10:30 UTC. The ash plume height reached up to 9.0 km a.s.l. In order to calculate the a-priori emissions, the data were resampled at ~2-hour intervals, specifically at 6:00, 8:00 and 10:00 UTC. During the initial hours of the eruption (6:30 - 7:45 UTC) the ash plume was weak (Figure 1, a) with an average column injection height of 5.8 km, resulting in an estimated MER of approximately 12,000 kg/s according to the equation by Mastin et al., (2009) (Table 3). After 07:45 UTC, a stronger plume formatted extending vertically above the vent (Figure 1 b). The ash plume exceeded the ECV camera field of view (e.g., more than 9.0–9.5 km a.s.l.) and was particularly strong between 08:00 – 09:45 UTC (Figure 1 c). The MER during this period averaged 75,000 kg/s, with a mean plume height of 10 km a.s.l. The standard deviation of the mean MER indicates considerable inconsistency in the emissions, as the MER can change rapidly during an eruption due to fluctuations in the eruptive dynamics, such as the collapse of the eruption column. (Table 3).

The ash plume height began to decrease several minutes after the lava fountain ceased (Figure 1 d), with its disappearance becoming evident only after 10:15 UTC (Figure 1 d). The MER during this phase (10:00 - 10:30 UTC) was approximately 6,300 kg/s (Table 3). The maximum plume elevation was not recorded by the ECV camera due to its limited field of view (approx. 9.0 – 9.5 km a.s.l. as noted by Simona Scollo et al., 2014)), but according to SEVIRI aboard the geostationary Meteosat Second Generation satellite, the plume top height at 08:30 UTC was estimated at 11.5 km a.s.l. (Calvari et al., 2021).

Table 3: A-priori source vector x^a

Time (UTC)	Mean Column Height (m)	Mean Mass Eruption Rate (MER) (kg/s)	Standard deviation (std) of Mean MER (kg/s)
2021-03-12 06:00:00	5850	12,000	10,200
2021-03-12 08:00:00	10012	58,800	35,000
2021-03-12 10:00:00	5300	6,320	5,120

https://doi.org/10.5194/egusphere-2024-3181
Preprint. Discussion started: 3 January 2025

4. Results

On 12th of March 2021 the Etna volcanic plume was captured over the PANGEA-NOA observatory by the Polly^{XT} lidar system (Baars et al., 2017; Engelmann et al., 2016). A three-hour time window from 18:30 to 21:30 UTC, was selected to calculate aerosol optical properties using the Raman method (Ansmann et al., 2011). This time-window was chosen based both on the lidar observations and on FLEXPART simulations, which also indicated the presence of ash particles over the PANGEA-NOA station during this period. Figure 2 shows the time-height evolution of Polly^{XT} lidar measurements, depicting a dense aerosol layer between 8 and 12.5 km, with the majority of the ash plume (large, depolarizing aerosols) being confined in the altitudes between 9 to 11 km approximately 11 hours after the eruption (18:30 – 21:30 UTC). The layer is associated with volcanic ash advection from Etna, as indicated by the high particle linear depolarization ratios (40 – 50 % at the center of the plume), which are typical of non-spherical volcanic ash particles (Groß et al., 2013; Miffre et al., 2011; Pisani et al., 2012), (Figure 2 b).

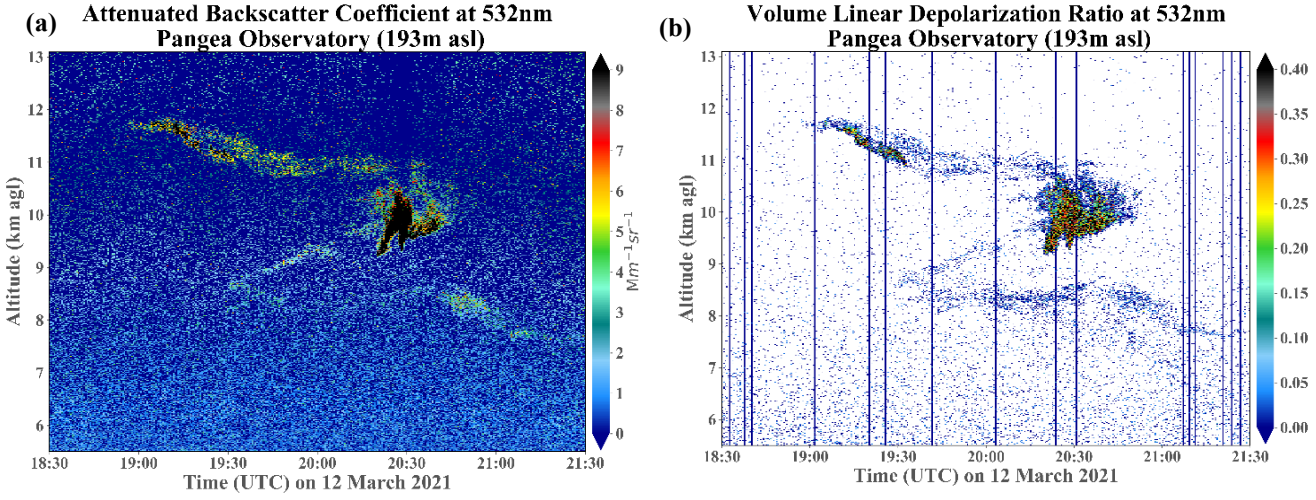

Figure 2: (a) The time-height curtain plot of the attenuated backscatter coefficient and (b) the volume linear depolarization ratio at 532 nm based of Polly^{XT} lidar observations at the PANGEA-NOA observatory during the 12th of March 2021 (18:30 to 21:30 UTC). Station elevation is at 193 m a.s.l.

To further analyze the volcanic plume distribution, Figure 3 presents the mass eruption rates in kg/s for both the a-priori (represented by circles) and a-posteriori (represented by stars) values, plotted as a function of ash plume height (m) and eruption time (UTC). The a-posteriori ash particle emissions in the "w" Aeolus simulation (Figure 3 a, b), obtained through the inversion scheme presented herein, were used as input for a new FLEXPART forward run. As discussed in Sect. 3.4.1, the a-priori MER (Figure 3 a, b) for ash particles was determined using the approach outlined by Scollo et al., (2019). The a-priori MER was obtained by inverting observed plume heights from the VONA reports, based on data collected by calibrated cameras operated by the INGV-EO observatory on 12th of March 2021, between 6:30 and 10:30 UTC. The ash plume's disappearance becomes noticeable only after 10:15 UTC (Figure 1d).

https://doi.org/10.5194/egusphere-2024-3181
Preprint. Discussion started: 3 January 2025

The a-priori MER values represented by circles, exhibit significant variability throughout the eruption period on 12 March 2021, between 06:30 and 10:30 UTC. Peak MER values, approaching 80,000 kg/s, are observed at approximately 12 km altitude between 09:30 and 09:45 UTC. Additionally, notable peaks occur at lower altitudes between 08:15 and 09:00 UTC, where MER values reach approximately 45,000 kg/s at around 9 km altitude (Figure 3 a, b).

In contrast, the a-posteriori MER values, denoted by stars, display a more constrained and consistent pattern, with lower magnitudes across most altitudes and times with respect to the a-priori estimates. The maximum a-posteriori MER reaches approximately 45,000 kg/s at an altitude of 10.5 km, occurring between 08:15 and 08:45 UTC (Figure 3 a, b).

A notable distinction between the two sets of emission estimates is the greater spread of the a-priori emissions across a wider range of altitudes, with values often exceeding those of the a-posteriori emissions. This is especially evident at lower altitudes (below 7 km) (Figure 3 b, c), where relative differences range between 40 % and 80 % from 06:30 to 07:45 UTC. These differences suggest an overestimation of the initial a-priori emissions obtained by inverting observed plume heights from the VONA reports, compared to the ash emissions derived from the inversion scheme (Figure 3 c).

On the other hand, the a-posteriori MER values present a more refined and clustered distribution between 7 and 12.5 km altitude (Figure 3 a), indicating a more constrained and likely more accurate estimation of ash emissions. This contrast is particularly evident when compared to the more scattered and variable a-priori estimates.

Between 10:00 and 10:30 UTC both a-priori and a-posteriori estimates indicate a distinct decline in MER, with values dropping below 10,000 kg/s at lower altitudes (~5 km). During this period, the relative differences between plume height and MER exceed 80 %, highlighting the divergence between the initial and adjusted estimates (Figure 3 c).

Regarding the ash plume height, the a-posteriori estimates consistently indicate higher altitudes compared to the a-priori estimates, a discrepancy potentially attributed to the limited field of view of the calibrated camera from the INGV-EO observatory. The camera's restricted range (approximately 9.0 – 9.5 km a.s.l., as noted by Simona Scollo et al., 2014) may have failed to capture the full extent of the plume, leading to underestimations in the a-priori estimates.

Additionally, Calvari et al., (2021) in their results further indicate that the observed plume column altitudes predominantly range between 6 and 9 km, which is the upper limit of the INGV-OE camera system. As a result, column heights exceeding 9 km a.s.l. are likely limited, contributing to differences between a-priori and a-posteriori estimates.

https://doi.org/10.5194/egusphere-2024-3181
Preprint. Discussion started: 3 January 2025

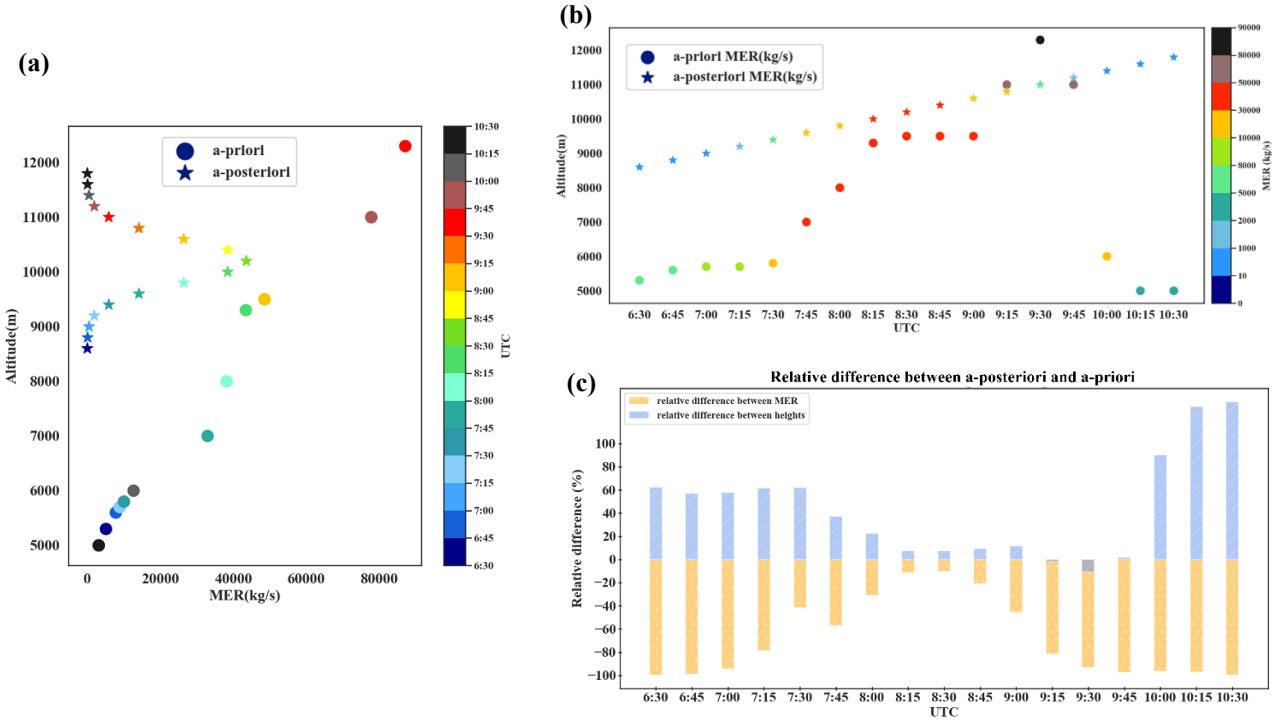

Figure 3: A-priori and a-posteriori ash emissions. (a) Comparison of temporally averaged vertical profiles of ash emissions used a priori (circles) and obtained a posteriori by the inversion (stars). The colorbar indicates the corresponding times of eruption, (on 12th of March 2021, from 6:30-10:30 UTC), each color representing a specific time; (b) A-priori (circles) and a-posteriori (stars) MER (unit kg/s) as a function of altitude (m) and time (UTC), on 12th of March 2021 from 6:30 - 10:30 UTC. The colorbar indicates the corresponding MER values, (from 0 to 90,000 kg/s), each color representing a specific MER range. The time axis reflects the period during which the ash plume was recorded by the ECV calibrated camera (6:30 - 10:30 UTC); (c) Relative differences (%) between a-posteriori and a-priori for ash emissions (orange columns) and plume height (blue columns) as a function of time (UTC). All heights are given in meters above sea level.

The relative differences between the two estimates are notably smaller, ranging from 10 % to 40 % between 08:00 and 09:00 UTC (Figure 3 c), suggesting a reasonable agreement between the a-priori and a-posteriori assessments for both emissions and column heights during this time window of the eruptive phase.

This improvement in the a-posteriori profile underscores the efficacy of the inversion algorithm in producing a more reliable representation of the vertical distribution of the ash emissions by improving the precision of eruption source parameters. The a-posteriori MER profile alignment with the observational data suggests that this method provides a robust and realistic assessment of ash emissions, particularly in the critical altitude range where volcanic plumes typically occur (Degruyter and Bonadonna, 2012; Mastin et al., 2009; Scollo et al., 2019).

https://doi.org/10.5194/egusphere-2024-3181
Preprint. Discussion started: 3 January 2025

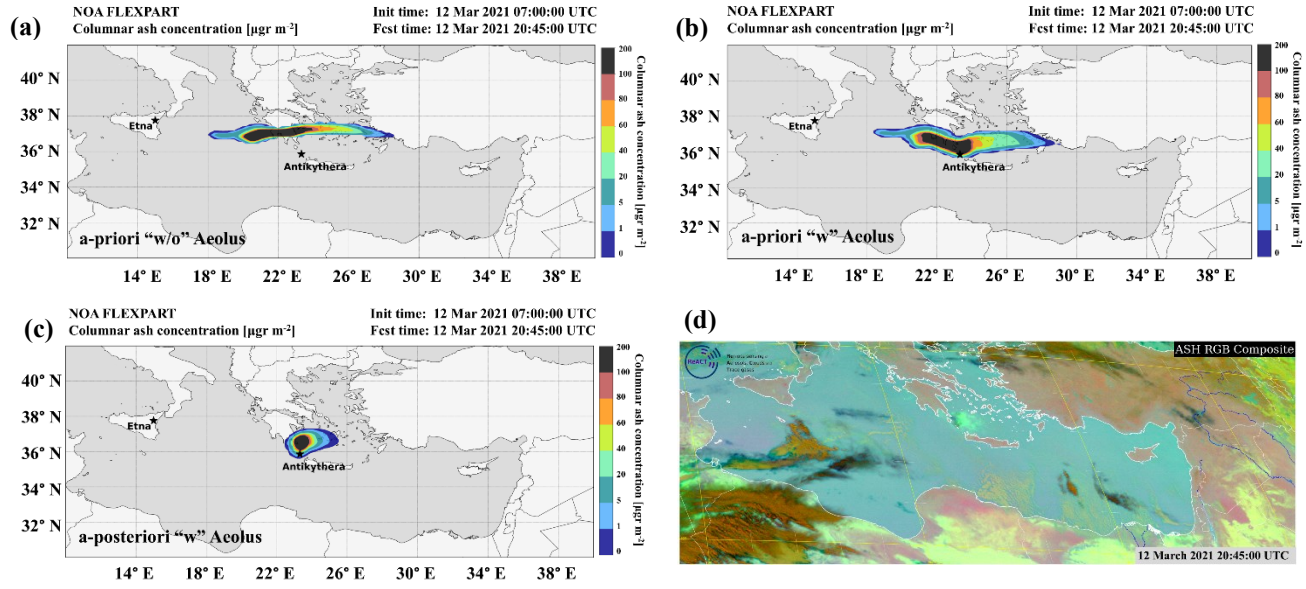

Figure 4: FLEXPART simulations of the volcanic ash. (a) a-priori ash column loading (μgr/m^2), using meteorological fields "w/o", and (b) "w" Aeolus wind assimilation; (c) a-posteriori ash column loading (μgr/m^2), using meteorological fields "w", (12th of March 2021, 20:45 UTC); (d) EUMETSAT Meteosat-11 volcanic Ash (RGB-MSG-0-degree) product of the ash plume derived from the Spinning Enhanced Visible and InfraRed Imager (SEVIRI), during paroxysmal activity at Mt. Etna on 12th of March 2021. Composite thermal IR (8.7, 10.8, 12 wavelengths) satellite image from the SEVIRI captures the volcanic ash plume about 11 hours after the start of the eruption above the PANGEA-NOA station, at Antikythera island in Greece, on 12th of March 2021, 20:45 UTC. SEVIRI data can downloaded from the EUMETSAT data portal (https://view.eumetsat.int/productviewer?v=default).

The FLEXPART simulated a-priori distribution (μg/m^2) of the ash clouds over the Eastern Mediterranean at 20:45 UTC, using meteorological fields "w/o" and "w" Aeolus wind assimilation is shown in Figure 4 (a, b). The ash plume is shown to arrive over Antikythera from the west, only when Aeolus assimilated wind fields were used (Figure 4 b). In contrast, the volcanic plume in the "w/o" Aeolus forecast never crosses Antikythera, as the forecasted cloud displaced to the north (Figure 4 a). Additionally, the a-posteriori distribution of the ash plume transport (μg/m^2) over the Eastern Mediterranean at 20:45 UTC, using Aeolus wind assimilation, is shown in Figure 4 (c). However, the a-posteriori particle emission rates in the "w/o" Aeolus simulation, could not be estimated from the inversion scheme due to very low source-receptor relationships derived from the FLEXPART model (see Appendix A, Figure A 1 right panel). As a result, the a-posteriori simulation of ash plume transport "w/o" Aeolus assimilation was not produced.

https://doi.org/10.5194/egusphere-2024-3181
Preprint. Discussion started: 3 January 2025

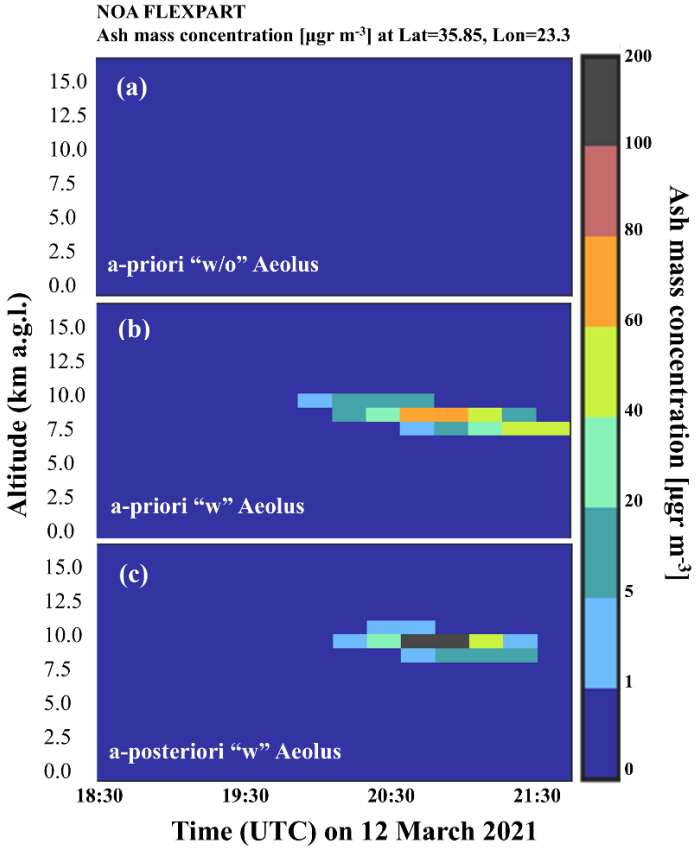

405 **Figure 5: FLEXPART time-height cross-sections on the 12th of March 2021, 18:30 – 21:30 UTC, over the PANGEA observatory in Antikythera, Greece. (a) time-height plot of a-priori FLEXPART volcanic ash concentrations over Antikythera "w/o" Aeolus wind assimilation over Antikythera, Greece (zero values); (b) time-height plot of a-priori FLEXPART volcanic ash concentrations over Antikythera "w" Aeolus wind assimilation; (c) time-height plot of a-posteriori FLEXPART volcanic ash concentrations over Antikythera "w" Aeolus wind assimilation over Antikythera, Greece ("w/o" are not calculated).**

410 The a-posteriori ash plume is notably more concentrated than the a-priori plume (Figure 4 b and c) and covers a smaller area, mostly limited to the area around Antikythera and southern Greece. In contrast, the a-priori ash plume (Figure 4 b) is more widely dispersed potentially due to the higher MER values (Figure 3 a denoted as circles) leading to an overestimation of the a-priori ash emissions. The a-priori ash plume dispersion extends from the eastern coast of Greece and reaches as far as the western islands. Furthermore, the structure of the a-posteriori ash plume closely resembles the ash cloud image captured by
415 the EUMETSAT Meteosat-11 Ash RGB product from the SEVIRI satellite, above Antikythera island on 12th of March 2021, at 20:45 UTC (Figure 4 d), again highlighting the importance of constraining the variability of the simulation results towards a more stable solution.

A thorough evaluation of the different model simulations is performed against the quality-assured lidar measurements of the PANGEA-NOA observatory. Figure 5 represents the vertical profiles of the FLEXPART simulated ash mass concentrations
420 over PANGEA-NOA. FLEXPART vertical time-height cross-sections of volcanic ash a-priori and a-posteriori concentrations

https://doi.org/10.5194/egusphere-2024-3181
Preprint. Discussion started: 3 January 2025

"w" Aeolus assimilated fields (Figure 5 b, c) show a similar pattern to the observed volcanic aerosol layer over Antikythera (Figure 2 a) but reveal significant differences in the vertical distribution and ash mass concentrations.

Specifically, the a-priori simulation using "w" Aeolus wind assimilation, forecasts a volcanic ash layer at an altitude range of approximately 7.5 to 11 km a.s.l., with ash concentrations reaching bellow to 100 μg/m³ over Antikythera between 18:30 UTC and 21:30 UTC (Figure 5 b). In contrast, the a-priori run "w/o" Aeolus assimilation fails to capture the observed ash particle concentrations over Antikythera (Figure 5 a). In the a-posteriori simulation, the ash plume driven by the "w" Aeolus wind fields is notably more aligned and better defined than in the a-priori simulation with respect to the observed ash plume (Figure 5 c) and (Figure 2). The a-posteriori profile reveals a volcanic ash layer at an altitude range of 7.5 to 12.5 km with higher ash concentrations, than in the a-priori layer, reaching up to 200 μg/m³ over Antikythera during the same time period (Figure 5 c). Notably, in the a-posteriori profile (Figure 5 c), the main part of the ash plume with the highest concentrations is confined between 9 and 11 km, consistent with the observed lidar profile (Figure 2 a). However, the a-posteriori FLEXPART time-height cross-sections using the "w/o" Aeolus wind fields were not calculated, as the a-posteriori emission rates could not be estimated by the inversion scheme due to very low SRR derived from the FLEXPART model (see Appendix A, Figure A 1 right panel).

This enhancement in both the vertical distribution and the concentration of the volcanic ash in the a-posteriori simulation (Figure 5 c), compared to the time-height profile of the observed ash plume derived from Polly^{XT} lidar, on 12th of March from 18:30 to 21:30 UTC (Figure 2 a), highlights the effectiveness of the inversion process when utilizing Aeolus wind data.

The aerosol optical properties profiles retrieved from the lidar data, are shown in Figure 6. The POLIPHON method as described in Sect. 3.1.1. was utilized to derive the pure-ash mass concentration profiles.

Polly^{XT} lidar retrievals show that the volcanic ash concentrations over PANGEA-NOA reached up to almost 250 ± 80 μg/m^3 at the plume's center of mass which is estimated at 10 km (orange line at Figure 6 c and Figure 7). The uncertainty in mass concentration calculation is marked with a black error bar in Figure 6 a.

https://doi.org/10.5194/egusphere-2024-3181
Preprint. Discussion started: 3 January 2025

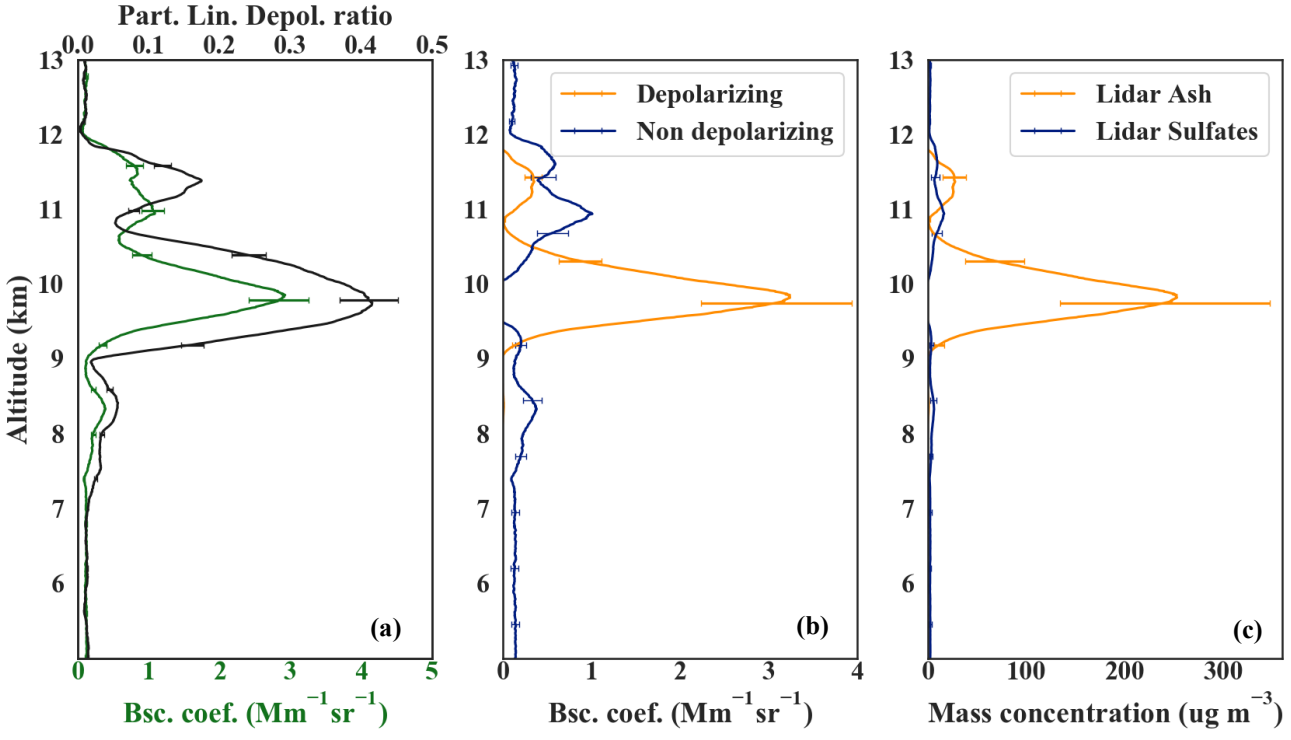

Figure 6: Lidar-derived optical properties over the PANGEA observatory on the 12th of March 2021 (18:30 – 21:30 UTC). Vertical distributions of: (a) total backscatter coefficient (green line) and particle linear depolarization ratio at 532 nm (black line); (b) depolarizing (orange line) and non-depolarizing (blue line) particle backscatter coefficient; (c)Volcanic mass concentrations using the POLIPHON method for ash (orange line) and sulfates (blue line).

The a-posteriori ash emissions from the "w" Aeolus simulation, obtained through the inversion scheme (Figure 3, stars), were used as input for a new FLEXPART forward run. This run was conducted to estimate a-posteriori ash mass concentrations above the PANGEA-NOA station between 18:30 and 21:30 UTC, focusing on fine ash particles with diameter of 3, 5, 9, and 21 μm.

Figure 7 compares the vertical profiles of the observed and the simulated (a-priori and a-posteriori "w" Aeolus assimilation) volcanic ash concentrations. The a-priori and a-posteriori ash mass concentrations "w/o" Aeolus simulation equals to zero and are not shown.

The corresponding mass concentrations derived from FLEXPART a-priori simulation (green line) and a-posteriori simulation (blue line) are shown in Figure 7 for comparison with the lidar observations (orange line).

The a-priori simulation produced ash concentrations of approximately 150 - 180 μg/m³ at the plume's center of mass, at 8.5 km (green line in Figure 7). While the a-priori profile shows good spatio-temporal agreement with the lidar retrievals (orange line in Figure 7), there is a slight vertical shift of 1 km between the modeled and observed ash mass peaks, which is critical for aviation safety. Furthermore, there is a misfit of about 50 μg/m^3 between the ash concentrations derived by the Polly^{XT} lidar and those reproduced by the model in the a-priori simulation, even with Aeolus data assimilated.

https://doi.org/10.5194/egusphere-2024-3181
Preprint. Discussion started: 3 January 2025

In contrast, when comparing the modeled a-posteriori ash mass concentrations to the lidar observations their agreement is evident when Aeolus winds are assimilated. The maximum ash mass concentration is approximately 250 µg/m^3 at 9.8 km, closely matching the peak observed by the lidar, while also the vertical distribution of the ash plume is depicted with high accuracy. The difference between the observed and the a-posteriori simulated ash mass concentrations is minimal and only 2 %. In contrast, the difference between the lidar observations and the a-priori ash simulations ranged from 28% to 40%. This demonstrates that the estimated emission profile obtained from the inversion algorithm that presented herein is remarkably robust. Overall, the inversion profile yields a much better agreement with lidar observations, confirming the effectiveness of the inversion process and the value of incorporating Aeolus wind data into the model.

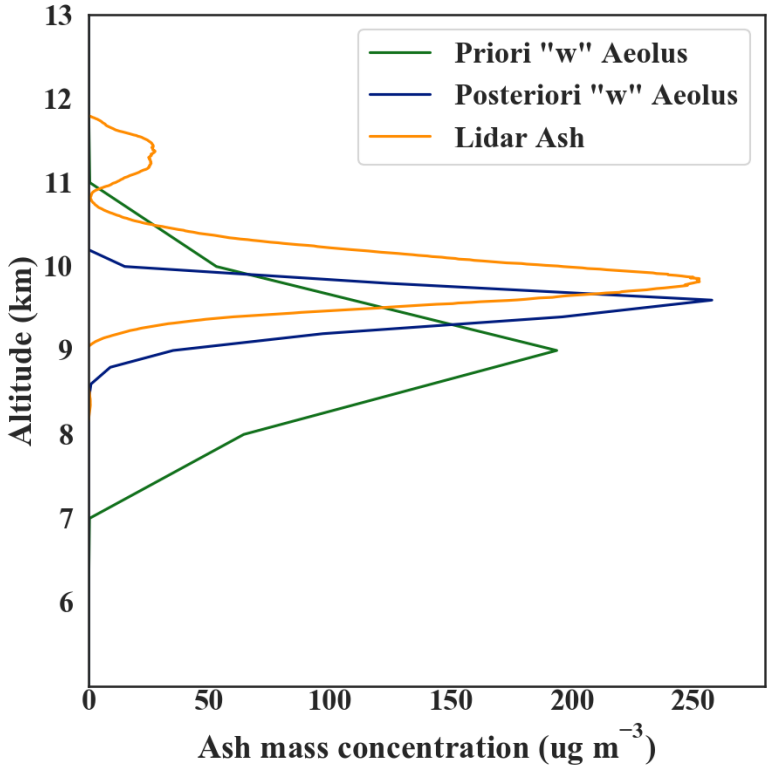

Figure 7: Vertical profile of volcanic ash concentration above PANGEA-NOA station on 12th of March 2021 between 18:30 to 21:30 UTC following the Inversion. Volcanic ash mass concentrations using the POLIPHON method (orange line); FLEXPART a-priori model simulations "w" Aeolus assimilated winds (green line), for the fine particles (3, 5, 9, and 21 µm diameter); FLEXPART a-posteriori model simulations "w" Aeolus assimilated winds (blue line), for the fine particles (3, 5, 9, and 21 µm diameter); a-priori and a-posteriori ash mass concentrations "w/o" Aeolus simulation equals to zero and are not shown.

5. Conclusions and discussion

The present study presented an inversion method to estimate the volcanic emission rate profile with a Lagrangian particle dispersion model and a ground-based lidar system. The technique was applied to the case study of the explosive eruption of

https://doi.org/10.5194/egusphere-2024-3181
Preprint. Discussion started: 3 January 2025

Mt. Etna, Italy, on 12th of March 2021. To assess the impact of Aeolus wind assimilation in volcanic ash dispersion forecasts, the experiment was repeated twice: once with Aeolus data assimilated ("w" experiment) and once without ("w/o"). The volcanic aerosol layers observed above the PANGEA-NOA station in Antikythera, along with the predominantly cloud-free conditions in the days following the eruption, made this an ideal test case. Important conclusions from our work are as follows: The Polly^{XT} lidar system of PANGEA-NOA detected a dense aerosol layer between 8 and 12.5 km, with the volcanic ash plume primarily concentrated between 9 and 11 km. FLEXPART simulations, both a-priori (with an empirical emission profile) and a-posteriori (with the emission profile produced by the inversion algorithm), were conducted to derive the modeled plumes vertical distribution and concentration. The a-priori "w" Aeolus simulation showed a broader dispersion of the ash plume potentially due to the overestimation of the a-priori ash emissions obtained by inverting observed plume heights from the VONA reports, whereas the a-posteriori simulation, based on the inversion results, produced a more refined and consistent ash plume profile, confined to a smaller area, mostly around Antikythera and southern Greece, closely similar to the ash cloud observed by the SEVIRI satellite.

In terms of ash mass concentration, the a-priori profile with Aeolus wind data assimilated, shows a good spatio-temporal agreement with the lidar retrievals but exhibited a slight vertical shift of 1 km with respect to the observed ash mass peaks along with a misfit in mass concentrations of about 50 μg/m^3, a critical factor for aviation safety. In contrast, the a-posteriori ash mass concentrations demonstrate a better agreement with the observations above PANGEA when Aeolus winds are assimilated. The maximum ash mass concentration is found close to 255 μg/m^3 at 9.8 km, closely matching the peak observed by the lidar, depicting a minimal difference of the order of 2 % between the observed and the a-posteriori simulated ash mass concentrations. In contrast, the difference between the lidar observations and the a-priori ash simulations ranged from 28% to 40%. This consistency highlights the robustness of the new inversion algorithm and the significant improvement in the vertical distribution and the ash mass concentration.

The accuracy of the FLEXPART a-posteriori simulation is highly dependent on the precision of the driving meteorological fields ("w" Aeolus wind fields), as well as on volcano source parameters such as the plume height and the mass eruption rates, which are refined through the inversion process (a-posteriori MER).

The advantages of Aeolus wind assimilation for global NWP models have been well documented, particularly by Rennie et al. (2021), who demonstrated significant improvements in wind field representation, especially in the Tropics and Southern Hemisphere. Further enhancements in wind forecasts were observed in the study of Amiridis et al. (2023), where regional NWP models benefited from Aeolus wind assimilation. Our case study validates these findings, showing that the assimilation of Aeolus wind profiles leads to a significant improvement in the estimation of volcanic emission rates in the vertical distribution, optimizing the agreement between lidar observations and a-posteriori model simulation.

Real-time applications, such as those of VAACs, demand a rapid response to volcanic ash hazards. Once the plume is detected and initial data from lidar systems become available, the presented method can quickly provide the necessary information to calculate the current and future position and extent of the plume within a few hours. This underscores the imperative for high-quality, rapidly accessible data, such as that provided by organized ground-based lidar networks employing standardized

https://doi.org/10.5194/egusphere-2024-3181
Preprint. Discussion started: 3 January 2025

algorithms and procedures, such as those used by EARLINET a key component of the ACTRIS infrastructure. It is also important to mention that the methodology presented herein can be applied to current or future satellite missions that employ lidar measurements (e.g. the EarthCARE mission). While passive satellites offer near-global coverage of ash cloud measurements within minutes to hours, ground-based or satellite lidar systems provide more accurate direct retrievals of the vertical distribution within the ash plume column.

Our methodology is broadly applicable and efficient enough for real-time implementation. It can supply ash forecasting models with an objectively derived quantitative source term, leading to improved forecasts that are critical for the aviation sector. These enhanced forecasts provide more effective emergency responses, ensuring safer and more efficient flight operations during volcanic eruptions, while at the same time minimizing the risk of accidents and the financial impact of flight cancellations.

Appendix A

The SRR for a size distribution of volcanic ash particles with four size bins (3, 5, 9, and 21 μm diameter), derived from the FLEXPART model, using the "w" Aeolus assimilated wind fields, indicate that the volcanic emissions observed above the PANGEA-NOA observatory (receptor - y axis) on 12th of March 2021 (from 18:30 to 21:30 UTC) at the height range 6 - 12 km mostly originate from release heights between 5 and 11.5 km above the Etna volcano (source – x axis) (Figure A 1, left). These source release heights are consistent with the observed emissions above the PANGEA-NOA station, particularly when the particle release time was 06:00 - 08:00 and 08:00 - 10:00 UTC. The source heights for the fine particles align well with the eruptive column heights, as reported from the INGV-OE calibrated cameras (Figure 1). Additionally, the inversion algorithm was utilized with the FLEXPART SRR only for these two release times. In contrast, the SRR using "w/o" Aeolus assimilated wind fields show that the volcanic particles arriving above the PANGEA station at heights of 8 – 10 km (receptor y axis) are few and originate from release heights around 8 - 11 km above Etna (source x axis) and only when the particle release time was 04:00 - 06:00 UTC (Figure A 1, right). This release time is not accurate, as the eruption actually began at 06:00 UTC according to the VONA messages from INGV-EO.

https://doi.org/10.5194/egusphere-2024-3181
Preprint. Discussion started: 3 January 2025

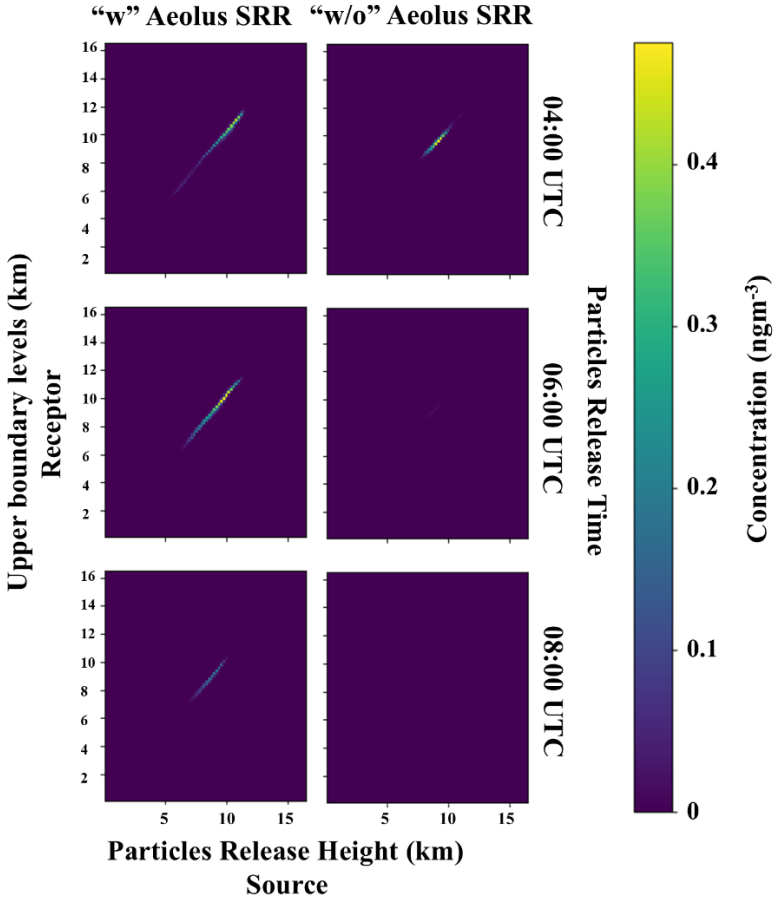

Figure A 1: Source-Receptor sensitivities for the fine particles (3, 5, 9, and 21 µm diameter) "w" Aeolus assimilated winds (left panel) and "w/o" Aeolus simulation (right panel). The horizontal axis "x" depicts the particles release height (km) above Etna and the vertical axis "y" is the altitude above PANGEA that the emissions observed on 12th of March 2021 (18:30 to 21:30 UTC).

Code availability

The inversion algorithm was written with Python programming language version 3.12 (https:// www. python. org/) and can be obtained from the author Anna Kampouri (akampouri@noa.gr) upon request. The WRF model code is publicly available, has a digital object identifier https:// doi. org/ 10. 5065/ D6MK6 B4K and can be obtained via GitHub (https:// github. com/ wrf-model/ WRF). The FLEXPART-WRF model code is publicly available and can be obtained from https:// www. flexp art. eu/ wiki/ FpOth ermet input. The code used for data processing was written with Python programming language version 3.12 (https:// www. python. org/) and can be obtained via GitHub: (https:// github. com/ NOA- ReACT/ Aeolus_Volcano_ 2023). The retrievals and the aerosol lidar optical properties are available from the co-author Anna Gialitaki (togialitaki@noa.gr) upon request.

https://doi.org/10.5194/egusphere-2024-3181
Preprint. Discussion started: 3 January 2025

Data availability

The Aeolus L2A wind data can be downloaded from: https://apps.ecmwf.int/mars-catalogue/?class=rd&expver=hkv, (ECMWF, 2021) (last access October 2024). The lidar data from the Polly^{XT} at PANGEA station (i.e., attenuated backscatter coefficient and volume linear depolarization ratio), were derived using the Single Calculus Chain (SCC; https:// scc. imaa. cnr. it) algorithm; an automatic-analysis tool for lidar data processing, developed within EARLINET (https:// www. earli net. org/) and ACTRIS (https:// www. actris. eu/) and are available by the co-author Anna Gialitaki (togialitaki@noa.gr) upon request. The WRF and FLEXPART-WRF models simulation results are also available by the author Anna Kampouri (akampouri@noa.gr) upon request.

Author contributions

A.K. conceptualized the manuscript along with V.A., P.Z. and S.So. (Stavros Solomos). All authors wrote parts of the manuscript corresponding to their work and respective results. A.K. performed the FLEXPART and WRF runs along and the inversion algorithm with the support of S.So., P.Z., and T.G.. A.G. and MT, provided the Polly^{XT} lidar retrievals. S.Sc. (Simona Scollo) provided the INGV-OE camera material and synergistic datasets for the analysis. M.R. provided the ECMFW IFS datasets ("w" and "w/o" Aeolus assimilation). All authors provided corrections and suggestions to eventually shape the research, analysis, and the final manuscript. A.K. supervised and directed the whole project.

Competing interests

The authors declare that they have no conflict of interest.

Disclaimer

Publisher's note: Copernicus Publications remains neutral with regard to jurisdictional claims in published maps and institutional affiliations.

Special issue statement

This article is part of the special issue "Aeolus data and their application (AMT/ACP/WCD inter-journal SI)". It is not associated with a conference.

https://doi.org/10.5194/egusphere-2024-3181
Preprint. Discussion started: 3 January 2025

Acknowledgements

AK and the authors affiliated to the National Observatory of Athens acknowledges the support by the following research projects: the PANGEA4CalVal project funded by the European Union (Grant Agreement 101079201); the e-shape project, under the European Union's Horizon 2020 research and innovation programme (Grant Agreement 820852); The ACTRIS Research Infrastructure; data and services obtained from the PANhellenic GEophysical Observatory of Antikythera (PANGEA) of NOA; Additionally, AK and TG acknowledges support by ESA in the framework of the "Enhancing Aeolus L2A for depolarizing targets and impact on aerosol research and NWP project (4000139424/22/I-NS).

AK acknowledges the support by Ioannis Binietoglou, Antonis Gkikas and Emmanouil Proestakis for their invaluable assistance and insightful discussions throughout the development of this work.

References

Amiridis, V., Kampouri, A., Gkikas, A., Misios, S., Gialitaki, A., Marinou, E., Rennie, M., Benedetti, A., Solomos, S., Zanis, P., Vasardani, O., Eleftheratos, K., Paschou, P., Georgiou, T., Scollo, S., Mona, L., Papagiannopoulos, N., Retscher, C., Parrinello, T., and Straume, A. G.: Aeolus winds impact on volcanic ash early warning systems for aviation, Sci Rep, 13, 7531, https://doi.org/10.1038/s41598-023-34715-6, 2023.

INGV-EO: https://www.ct.ingv.it/.

Ansmann, A., Petzold, A., Kandler, K., Tegen, I., Wendisch, M., Müller, D., Weinzierl, B., Müller, T., and Heintzenberg, J.: Saharan Mineral Dust Experiments SAMUM–1 and SAMUM–2: what have we learned?, Tellus B: Chemical and Physical Meteorology, 63, 403, https://doi.org/10.1111/j.1600-0889.2011.00555.x, 2011.

Ansmann, A., Seifert, P., Tesche, M., and Wandinger, U.: Profiling of fine and coarse particle mass: case studies of Saharan dust and Eyjafjallajökull/Grimsvötn volcanic plumes, Atmos. Chem. Phys., 12, 9399–9415, https://doi.org/10.5194/acp-12-9399-2012, 2012.

Baars, H., Seifert, P., Engelmann, R., and Wandinger, U.: Target categorization of aerosol and clouds by continuous multiwavelength-polarization lidar measurements, Atmos. Meas. Tech., 10, 3175–3201, https://doi.org/10.5194/amt-10-3175-2017, 2017.

Beckett, F., Rossi, E., Devenish, B., Witham, C., and Bonadonna, C.: Modelling the size distribution of aggregated volcanic ash and implications for operational atmospheric dispersion modelling, Atmos. Chem. Phys., 22, 3409–3431, https://doi.org/10.5194/acp-22-3409-2022, 2022.

Brioude, J., Arnold, D., Stohl, A., Cassiani, M., Morton, D., Seibert, P., Angevine, W., Evan, S., Dingwell, A., Fast, J. D., Easter, R. C., Pisso, I., Burkhart, J., and Wotawa, G.: The Lagrangian particle dispersion model FLEXPART-WRF version 3.1, Geosci. Model Dev., 6, 1889–1904, https://doi.org/10.5194/gmd-6-1889-2013, 2013.

Calvari, S., Bonaccorso, A., and Ganci, G.: Anatomy of a Paroxysmal Lava Fountain at Etna Volcano: The Case of the 12 March 2021, Episode, Remote Sensing, 13, 3052, https://doi.org/10.3390/rs13153052, 2021.

Chen, F. and Dudhia, J.: Coupling and advanced land surface-hydrology model with the Penn State-NCAR MM5 modeling system. Part I: Model implementation and sensitivity., Mon. Weather Rev., 129, 569–585, 2001.

https://doi.org/10.5194/egusphere-2024-3181
Preprint. Discussion started: 3 January 2025

Clarkson, R. and Simpson, H.: Maximising Airspace Use During Volcanic Eruptions: Matching Engine Durability against Ash Cloud Occurrence, 2017.

Corradini, S., Guerrieri, L., Lombardo, V., Merucci, L., Musacchio, M., Prestifilippo, M., Scollo, S., Silvestri, M., Spata, G., and Stelitano, D.: Proximal Monitoring of the 2011–2015 Etna Lava Fountains Using MSG-SEVIRI Data, Geosciences, 8, 140, https://doi.org/10.3390/geosciences8040140, 2018.

Dacre, H. F., Grant, A. L. M., Hogan, R. J., Belcher, S. E., Thomson, D. J., Devenish, B. J., Marenco, F., Hort, M. C., Haywood, J. M., Ansmann, A., Mattis, I., and Clarisse, L.: Evaluating the structure and magnitude of the ash plume during the initial phase of the 2010 Eyjafjallajökull eruption using lidar observations and NAME simulations, J. Geophys. Res., 116, D00U03, https://doi.org/10.1029/2011JD015608, 2011.

D'Amico, G., Amodeo, A., Baars, H., Binietoglou, I., Freudenthaler, V., Mattis, I., Wandinger, U., and Pappalardo, G.: EARLINET Single Calculus Chain – overview on methodology and strategy, Atmos. Meas. Tech., 8, 4891–4916, https://doi.org/10.5194/amt-8-4891-2015, 2015.

Degruyter, W. and Bonadonna, C.: Improving on mass flow rate estimates of volcanic eruptions, Geophysical Research Letters, 39, 2012GL052566, https://doi.org/10.1029/2012GL052566, 2012.

Dubovik, O., Sinyuk, A., Lapyonok, T., Holben, B. N., Mishchenko, M., Yang, P., Eck, T. F., Volten, H., Muñoz, O., Veihelmann, B., Van Der Zande, W. J., Leon, J., Sorokin, M., and Slutsker, I.: Application of spheroid models to account for aerosol particle nonsphericity in remote sensing of desert dust, J. Geophys. Res., 111, 2005JD006619, https://doi.org/10.1029/2005JD006619, 2006.

Durant, A. J., Bonadonna, C., and Horwell, C. J.: Atmospheric and Environmental Impacts of Volcanic Particulates, Elements, 6, 235–240, https://doi.org/10.2113/gselements.6.4.235, 2010.

Eckhardt, S., Prata, A. J., Seibert, P., Stebel, K., and Stohl, A.: Estimation of the vertical profile of sulfur dioxide injection into the atmosphere by a volcanic eruption using satellite column measurements and inverse transport modeling, 2008.

ECMWF: ECMWF Starts Assimilating Aeolus Wind Data., 2021.

Engelmann, R., Kanitz, T., Baars, H., Heese, B., Althausen, D., Skupin, A., Wandinger, U., Komppula, M., Stachlewska, I. S., Amiridis, V., Marinou, E., Mattis, I., Linné, H., and Ansmann, A.: The automated multiwavelength Raman polarization and water-vapor lidar Polly^{XT}: the neXT generation, Atmos. Meas. Tech., 9, 1767–1784, https://doi.org/10.5194/amt-9-1767-2016, 2016.

EUROCONTROL: Forecast Update 2022–2028, European Flight Movements and Service Units (2022)., 2022.

Fang, S., Dong, X., Zhuang, S., Tian, Z., Chai, T., Xu, Y., Zhao, Y., Sheng, L., Ye, X., and Xiong, W.: Oscillation-free source term inversion of atmospheric radionuclide releases with joint model bias corrections and non-smooth competing priors, Journal of Hazardous Materials, 440, 129806, https://doi.org/10.1016/j.jhazmat.2022.129806, 2022.

Fearnley, C. J., Bird, D. K., Haynes, K., McGuire, W. J., and Jolly, G. (Eds.): Observing the Volcano World: Volcano Crisis Communication, Springer International Publishing, Cham, https://doi.org/10.1007/978-3-319-44097-2, 2018.

Francis, P. N., Cooke, M. C., and Saunders, R. W.: Retrieval of physical properties of volcanic ash using Meteosat: A case study from the 2010 Eyjafjallajökull eruption, J. Geophys. Res., 117, 2011JD016788, https://doi.org/10.1029/2011JD016788, 2012.

https://doi.org/10.5194/egusphere-2024-3181
Preprint. Discussion started: 3 January 2025

Giles, D. M., Sinyuk, A., Sorokin, M. G., Schafer, J. S., Smirnov, A., Slutsker, I., Eck, T. F., Holben, B. N., Lewis, J. R., Campbell, J. R., Welton, E. J., Korkin, S. V., and Lyapustin, A. I.: Advancements in the Aerosol Robotic Network (AERONET) Version 3 database – automated near-real-time quality control algorithm with improved cloud screening for Sun photometer aerosol optical depth (AOD) measurements, Atmos. Meas. Tech., 12, 169–209, https://doi.org/10.5194/amt-12-169-2019, 2019.

Goloub, P., Li, Z., Dubovik, O., Blarel, L., Podvin, T., Jankowiak, I., Lecoq, R., Deroo, C., Chatenet, B., Morel, J. P., Cuevas, E., and Ramos, R.: PHOTONS/AERONET sunphotometer network overview: description, activities, results, SPIE Proceedings, 69360V-69360V–15, https://doi.org/10.1117/12.783171, 2007.

Groß, S., Esselborn, M., Weinzierl, B., Wirth, M., Fix, A., and Petzold, A.: Aerosol classification by airborne high spectral resolution lidar observations, Atmospheric Chemistry and Physics, 13, 2487–2505, https://doi.org/10.5194/acp-13-2487-2013, 2013.

Guffanti, M., Ewert, J. W., Gallina, G. M., Bluth, G. J. S., and Swanson, G. L.: Volcanic-ash hazard to aviation during the 2003–2004 eruptive activity of Anatahan volcano, Commonwealth of the Northern Mariana Islands, Journal of Volcanology and Geothermal Research, 146, 241–255, https://doi.org/10.1016/j.jvolgeores.2004.12.011, 2005.

Harvey, N. J., Dacre, H. F., Webster, H. N., Taylor, I. A., Khanal, S., Grainger, R. G., and Cooke, M. C.: The Impact of Ensemble Meteorology on Inverse Modeling Estimates of Volcano Emissions and Ash Dispersion Forecasts: Grímsvötn 2011, Atmosphere, 11, 1022, https://doi.org/10.3390/atmos11101022, 2020.

Houchi, K., Stoffelen, A., Marseille, G. J., and De Kloe, J.: Comparison of wind and wind shear climatologies derived from high-resolution radiosondes and the ECMWF model, J. Geophys. Res., 115, 2009JD013196, https://doi.org/10.1029/2009JD013196, 2010.

Iacono, M.J., Delamere, J.S., Mlawer, E.J., Shephard, M.W., Clough, S.A., and Collins, W.D.: Radiative forcing by long-lived greenhouse gases: Calculations with the AER radiative transfer models., J. Geophys. Res. Atmos., 113, 2–9, 2008.

ICAO: “Volcanic Ash Contingency Plan,” 2016.

Janjic: Nonsingular implementation of the Mellor-Yamada level 2.5 scheme in the NCEP Meso model., NCEP Off. Note, 437, 61, 2002.

Janjic, Z. I.: A nonhydrostatic model based on a new approach, Meteorology and Atmospheric Physics, 82, 271–285, https://doi.org/10.1007/s00703-001-0587-6, 2003.

Kampouri, A., Amiridis, V., Solomos, S., Gialitaki, A., Marinou, E., Spyrou, C., Georgoulias, A. K., Akritidis, D., Papagiannopoulos, N., Mona, L., Scollo, S., Tsichla, M., Tsikoudi, I., Pytharoulis, I., Karacostas, T., and Zanis, P.: Investigation of Volcanic Emissions in the Mediterranean: “The Etna–Antikythera Connection,” Atmosphere, 12, 40, https://doi.org/10.3390/atmos12010040, 2020.

Kampouri, A., Amiridis, V., Georgiou, T., Solomos, S., Binietoglou, I., Gialitaki, A., Marinou, E., Gkikas, A., Proestakis, E., Rennie, M., Benedetti, A., Scollo, S., Mona, L., Papagiannopoulos, N., and Zanis, P.: Inversion Techniques on Etna’s Volcanic Emissions and the Impact of Aeolus on Quantitative Dispersion Modeling, in: 16th International Conference on Meteorology, Climatology and Atmospheric Physics—COMECAP 2023, International Conference on Meteorology, Climatology and Atmospheric Physics, 187, https://doi.org/10.3390/environsciproc2023026187, 2023.

https://doi.org/10.5194/egusphere-2024-3181
Preprint. Discussion started: 3 January 2025

Konsta, D., Tsekeri, A., Solomos, S., Siomos, N., Gialitaki, A., Tetoni, E., Lopatin, A., Goloub, P., Dubovik, O., Amiridis, V., and Nastos, P.: The Potential of GRASP/GARRLiC Retrievals for Dust Aerosol Model Evaluation: Case Study during the PreTECT Campaign, Remote Sensing, 13, 873, https://doi.org/10.3390/rs13050873, 2021.

Kristiansen, N. I., Stohl, A., Prata, A. J., Richter, A., Eckhardt, S., Seibert, P., Hoffmann, A., Ritter, C., Bitar, L., Duck, T. J., and Stebel, K.: Remote sensing and inverse transport modeling of the Kasatochi eruption sulfur dioxide cloud, J. Geophys. Res., 115, 2009JD013286, https://doi.org/10.1029/2009JD013286, 2010.

Li, X., Li, H., Liu, Y., Xiong, W., and Fang, S.: Joint release rate estimation and measurement-by-measurement model correction for atmospheric radionuclide emission in nuclear accidents: An application to wind tunnel experiments, Journal of Hazardous Materials, 345, 48–62, https://doi.org/10.1016/j.jhazmat.2017.09.051, 2018.

Lopatin, A., Dubovik, O., Chaikovsky, A., Goloub, P., Lapyonok, T., Tanré, D., and Litvinov, P.: Enhancement of aerosol characterization using synergy of lidar and sun-photometer coincident observations: the GARRLiC algorithm, Atmos. Meas. Tech., 6, 2065–2088, https://doi.org/10.5194/amt-6-2065-2013, 2013.

Lopatin, A., Dubovik, O., Fuertes, D., Stenchikov, G., Lapyonok, T., Veselovskii, I., Wienhold, F. G., Shevchenko, I., Hu, Q., and Parajuli, S.: Synergy processing of diverse ground-based remote sensing and in situ data using the GRASP algorithm: applications to radiometer, lidar and radiosonde observations, Atmos. Meas. Tech., 14, 2575–2614, https://doi.org/10.5194/amt-14-2575-2021, 2021.

Mamouri, R.-E. and Ansmann, A.: Potential of polarization/Raman lidar to separate fine dust, coarse dust, maritime, and anthropogenic aerosol profiles, Atmos. Meas. Tech., 10, 3403–3427, https://doi.org/10.5194/amt-10-3403-2017, 2017.

Mastin, L. G., Guffanti, M., Servranckx, R., Webley, P., Barsotti, S., Dean, K., Durant, A., Ewert, J. W., Neri, A., Rose, W. I., Schneider, D., Siebert, L., Stunder, B., Swanson, G., Tupper, A., Volentik, A., and Waythomas, C. F.: A multidisciplinary effort to assign realistic source parameters to models of volcanic ash-cloud transport and dispersion during eruptions, Journal of Volcanology and Geothermal Research, 186, 10–21, https://doi.org/10.1016/j.jvolgeores.2009.01.008, 2009.

Mazzocchi, M., Hansstein, F., and Ragona, M.: The 2010 Volcanic Ash Cloud and Its Financial Impact on the European Airline Industry, 2010.

Miffre, A., David, G., Thomas, B., and Rairoux, P.: Atmospheric non-spherical particles optical properties from UV-polarization lidar and scattering matrix: NONSPHERICAL PARTICLES UV DEPOLARIZATION, Geophys. Res. Lett., 38, n/a-n/a, https://doi.org/10.1029/2011GL048310, 2011.

Näslund, E. and Thaning, L.: On the Settling Velocity in a Nonstationary Atmosphere, Aerosol Science and Technology, 14, 247–256, https://doi.org/10.1080/02786829108959487, 1991.

Oxford Economics.: The Economic Impacts of Air Travel Restrictions Due to Volcanic Ash. Prepared for Airbus., 2012.

Pavolonis, M. J., Heidinger, A. K., and Sieglaff, J.: Automated retrievals of volcanic ash and dust cloud properties from upwelling infrared measurements, JGR Atmospheres, 118, 1436–1458, https://doi.org/10.1002/jgrd.50173, 2013.

Petersen, G. N., Bjornsson, H., and Arason, P.: Two weather radar time series of the altitude of the volcanic plume during the May 2011 eruption of Grímsvötn, Iceland, 2011.

Pisani, G., Boselli, A., Coltelli, M., Leto, G., Pica, G., Scollo, S., Spinelli, N., and Wang, X.: Lidar depolarization measurement of fresh volcanic ash from Mt. Etna, Italy, Atmospheric Environment, 62, 34–40, https://doi.org/10.1016/j.atmosenv.2012.08.015, 2012.

https://doi.org/10.5194/egusphere-2024-3181
Preprint. Discussion started: 3 January 2025

Pisso, I., Sollum, E., Grythe, H., Kristiansen, N. I., Cassiani, M., Eckhardt, S., Arnold, D., Morton, D., Thompson, R. L., Groot Zwaaftink, C. D., Evangeliou, N., Sodemann, H., Haimberger, L., Henne, S., Brunner, D., Burkhart, J. F., Fouilloux, A., Brioude, J., Philipp, A., Seibert, P., and Stohl, A.: The Lagrangian particle dispersion model FLEXPART version 10.4, Geosci. Model Dev., 12, 4955–4997, https://doi.org/10.5194/gmd-12-4955-2019, 2019.

Pouget, S., Bursik, M., Webley, P., Dehn, J., and Pavolonis, M.: Estimation of eruption source parameters from umbrella cloud or downwind plume growth rate, Journal of Volcanology and Geothermal Research, 258, 100–112, https://doi.org/10.1016/j.jvolgeores.2013.04.002, 2013.

Prata, A. T., Grainger, R. G., Taylor, I. A., Povey, A. C., Proud, S. R., and Poulsen, C. A.: Uncertainty-bounded estimates of ash cloud properties using the ORAC algorithm: application to the 2019 Raikoke eruption, Atmos. Meas. Tech., 15, 5985–6010, https://doi.org/10.5194/amt-15-5985-2022, 2022.

Prata, F. and Lynch, M.: Passive Earth Observations of Volcanic Clouds in the Atmosphere, Atmosphere, 10, 199, https://doi.org/10.3390/atmos10040199, 2019.

Rennie, M. P., Isaksen, L., Weiler, F., De Kloe, J., Kanitz, T., and Reitebuch, O.: The impact of AEOLUS wind retrievals on ECMWF global weather forecasts, Quart J Royal Meteoro Soc, 147, 3555–3586, https://doi.org/10.1002/qj.4142, 2021.

Scollo, Michele Prestifilippo, Emilio Pecora, Stefano Corradini, Luca Merucci, Gaetano Spata, and Mauro Coltelli: Eruption column height estimation of the 2011-2013 Etna lava fountains, Annals of Geophysics, 57, 3, https://doi.org/10.4401/ag-6396, 2014.

Scollo, S., Prestifilippo, M., Bonadonna, C., Cioni, R., Corradini, S., Degruyter, W., Rossi, E., Silvestri, M., Biale, E., Carparelli, G., Cassisi, C., Merucci, L., Musacchio, M., and Pecora, E.: Near-Real-Time Tephra Fallout Assessment at Mt. Etna, Italy, Remote Sensing, 11, 2987, https://doi.org/10.3390/rs11242987, 2019.

Seibert, P. and Frank, A.: Source-receptor matrix calculation with a Lagrangian particle dispersion model in backward mode, Atmos. Chem. Phys., 2004.

Skamarock, W. C., Klemp, J. B., Dudhia, J., Gill, D. O., Barker, D. M., Duda, M. G., Huang, X.-Y., Wang, W., and Powers, J. G.: A Description of the Advanced Research WRF Version 4, 2019.

Stoffelen, A., Marseille, G. J., Bouttier, F., Vasiljevic, D., De Haan, S., and Cardinali, C.: ADM-Aeolus Doppler wind lidar Observing System Simulation Experiment, Q.J.R. Meteorol. Soc., 132, 1927–1947, https://doi.org/10.1256/qj.05.83, 2006.

Stoffelen, A., Benedetti, A., Borde, R., Dabas, A., Flamant, P., Forsythe, M., Hardesty, M., Isaksen, L., Källén, E., Körnich, H., Lee, T., Reitebuch, O., Rennie, M., Riishøjgaard, L.-P., Schyberg, H., Straume, A. G., and Vaughan, M.: Wind Profile Satellite Observation Requirements and Capabilities, Bulletin of the American Meteorological Society, 101, E2005–E2021, https://doi.org/10.1175/BAMS-D-18-0202.1, 2020.

Stohl, A., Forster, C., Frank, A., Seibert, P., and Wotawa, G.: Technical note: The Lagrangian particle dispersion model FLEXPART version 6.2, Atmos. Chem. Phys., 2005.

Stohl, A., Prata, A. J., Eckhardt, S., Clarisse, L., Durant, A., Henne, S., Kristiansen, N. I., Minikin, A., Schumann, U., Seibert, P., Stebel, K., Thomas, H. E., Thorsteinsson, T., Tørseth, K., and Weinzierl, B.: Determination of time- and height-resolved volcanic ash emissions and their use for quantitative ash dispersion modeling: the 2010 Eyjafjallajökull eruption, Atmos. Chem. Phys., 11, 4333–4351, https://doi.org/10.5194/acp-11-4333-2011, 2011.

https://doi.org/10.5194/egusphere-2024-3181
Preprint. Discussion started: 3 January 2025

Straume-Lindner, A. G., Parrinello, T., Von Bismarck, J., Bley, S., Wernham, D., Kanitz, T., Alvarez, E., Fischey, P., De Laurentis, M., Fehr, T., Ehlers, F., Duc Tran, V., Krisch, I., Reitebuch, O., and Renni, M.: ESA'S Wind Mission Aeolus - Overview, Status and Outlook, in: 2021 IEEE International Geoscience and Remote Sensing Symposium IGARSS, IGARSS 2021 - 2021 IEEE International Geoscience and Remote Sensing Symposium, Brussels, Belgium, 755–758, https://doi.org/10.1109/IGARSS47720.2021.9554007, 2021.

Thompson, G., Field, P. R., Rasmussen, R. M., and Hall, W. D.: Explicit Forecasts of Winter Precipitation Using an Improved Bulk Microphysics Scheme. Part II: Implementation of a New Snow Parameterization, Monthly Weather Review, 136, 5095–5115, https://doi.org/10.1175/2008MWR2387.1, 2008.

Wagner, J., Ansmann, A., Wandinger, U., Seifert, P., Schwarz, A., Tesche, M., Chaikovsky, A., and Dubovik, O.: Evaluation of the Lidar/Radiometer Inversion Code (LIRIC) to determine microphysical properties of volcanic and desert dust, Atmos. Meas. Tech., 6, 1707–1724, https://doi.org/10.5194/amt-6-1707-2013, 2013.

Weitkamp, C. (Ed.): Lidar: range-resolved optical remote sensing of the atmosphere, Springer, New York, NY, 455 pp., 2005.

Zhang, C., Wang, Y., and Hamilton, K.: Improved Representation of Boundary Layer Clouds over the Southeast Pacific in ARW-WRF Using a Modified Tiedtke Cumulus Parameterization Scheme*, Monthly Weather Review, 139, 3489–3513, https://doi.org/10.1175/MWR-D-10-05091.1, 2011.